nature climate change

Article

https://doi.org/10.1038/s41558-025-02308-y

Constrained Earth system models show a stronger reduction in future Northern Hemisphere snowmelt water

Received: 1 April 2024

Accepted: 6 March 2025

Published online: 28 March 2025

Check for updates

Yuanfang Chai[1], Chiyuan Miao[1] ✉, Pierre Gentine[2], Lawrence Mudryk[3], Chad W. Thackeray[4], Wouter R. Berghuijs[5], Yi Wu[1], Xuewei Fan[1], Louise Slater[6], Qiaohong Sun[7] & Francis Zwiers[7,8]

Although Earth system models (ESMs) tend to overestimate historical land surface warming, they also overestimate snow amounts in the Northern Hemisphere. By combining ground-based datasets and ESMs, we find that this paradoxical phenomenon is predominantly driven by an overestimation of light snowfall frequency. Using spatially distributed emergent constraints, we show that this paradox persists in mid- (2041–2060) and long-term (2081–2100) projections, affecting more than half of the Northern Hemisphere's land surface. ESMs underestimate the frequency of freezing days by 12–19% and overestimate snow water equivalent by 28–34%. Constrained projections indicate that the raw ESM outputs overestimate future Northern Hemisphere snowmelt water by 12–16% across 53–60% of the Northern Hemisphere's land surface. This snowmelt water overprediction implies that the amount of water available in the future for agriculture, industry, ecosystems and domestic use may be lower than unadjusted ESM projections suggest.

Terrestrial water is stored as snow in winter, and subsequently melts partially or completely during the spring and summer due to warming temperatures, releasing water through infiltration, which recharges soil moisture, or as runoff, which increases streamflow[1–11]. As the largest freshwater storage reservoir, snowmelt water is critical for domestic water supply, agriculture, hydroelectric power and ecosystems[5,12]. Snowmelt water in the Northern Hemisphere (NH) accounts for approximately one-third of all irrigation water[13], and supports one-fourth of global gross domestic product[12] and approximately one-sixth of Earth's population[14]. Decreases in snow volumes caused by global warming[15,16] are greatly affecting the hydrological cycle and are therefore often cited as a key threat to irrigated agriculture and food security[5–9,15–17]. Considering the importance of snow in shaping the global water cycle, a reliable understanding of the spatial dynamics of snow conditions in response to our warming climate is urgently required. This is especially true in the NH, which accounts for around 98% of global snow volume[18,19].

Recent studies have found considerable uncertainties in snow modelling across Earth system models (ESMs)[20,21]. These uncertainties underpin a 'snow water resources paradox' in the context of surface warming: Coupled Model Intercomparison Project phase 6 (CMIP6) and phase 5 (CMIP5) ESMs tend to overestimate historical warming trends[1–4] and underestimate the frequency of freezing days (days with

[1]State Key Laboratory of Earth Surface Processes and Resource Ecology, Faculty of Geographical Science, Beijing Normal University, Beijing, China. [2]Earth and Environmental Engineering, Climate School and Center for Learning the Earth with Artificial intelligence and Physics (LEAP), Columbia University, New York, NY, USA. [3]Climate Research Division, Environment and Climate Change Canada, Toronto, Ontario, Canada. [4]Department of Atmospheric and Oceanic Sciences, University of California, Los Angeles, Los Angeles, CA, USA. [5]Department of Earth Sciences, Vrije Universiteit Amsterdam, Amsterdam, Netherlands. [6]School of Geography and the Environment, University of Oxford, Oxford, UK. [7]Key Laboratory of Meteorological Disaster of Ministry of Education, Joint International Research Laboratory of Climate and Environment Change, Nanjing University of Information Science and Technology, Nanjing, China. [8]Pacific Climate Impacts Consortium, University of Victoria, Victoria, British Columbia, Canada. ✉e-mail: miaocy@bnu.edu.cn

daily mean temperature below 0 °C) when snowfall tends to occur, while overestimating snow water equivalent (SWE) relative to observations in recent decades[5–9]. We show that this paradox, which leads to the overestimation of annual snowmelt water, persists in future SWE and snowmelt water projections made with CMIP6 models. The future of NH SWE and snowmelt water resources remains unclear, given this paradox. This leads to confusion about future snow amounts as the climate warms[14,22,23], undermining estimations of future snow water resources and the ability of water management policies to address potential snow water resource shortages.

Emergent constraint methods can help reduce uncertainty in SWE and temperature projections arising from the snow water resources paradox[4,24–36]. By reducing these uncertainties, emergent constraints can help us assess whether the snow water resources paradox persists in the future projections, thus providing more reliable and accurate future snow projections for better management of future water resources. In this study, we introduce a spatially distributed hierarchical emergent constraint on future mid- (2041–2060) and long-term (2081–2100) NH SWE and freezing day frequency using 31 CMIP6 models (Supplementary Table 1) under four Shared Socioeconomic Pathway (SSP) emission scenarios (SSP126, SSP245, SSP370 and SSP585). Observationally constrained estimates of future SWE are then used to refine projections of future snowmelt water. These spatially constrained results help to better support the formulation of regional policies for water resources management that address local climate warming and environmental protection.

Snow water resources paradox over the historical period

Based on the Berkeley Earth land temperature record[37], we find that the frequency of freezing days is underestimated by the CMIP6 models (119 ± 19 days, ensemble mean ± s.d. of CMIP6 models) compared with observations (136 ± 4 days; Fig. 1a) in the extended NH cold season (excluding months from June to September) for the period 1982–2014. This underestimation occurs across more than nine-tenths of the NH's land surface (Fig. 1b, excluding snow-free regions).

Given that snowfall depends on both temperature and precipitation, a lower freezing day frequency in the CMIP6 ESMs implies reduced snow accumulation relative to observations. However, the CMIP6 models significantly overestimate ($P < 0.05$) the NH mean SWE (3,275 ± 1,279 Gt) by 50% compared with the observation-based estimate of 2,115 ± 777 Gt. This observation-based estimate is derived from nine SWE datasets (Supplementary Table 2): seven reanalysis datasets (Modern-Era Retrospective analysis for Research and Applications, Version 2 (MERRA-2), European Centre for Medium-range Weather Forecasts ReAnalysis 5-Land (ERA5-Land), Global Land Data Assimilation System Version 2 (GLDAS-v2), National Centers for Environmental Prediction Version 2 (NCEP2), Famine Early Warning Systems Network Land Data Assimilation System (FLDAS), Climate Forecast System Reanalysis (CFSR) and European Centre for Medium-range Weather Forecasts ReAnalysis 5 (ERA5)) and two satellite and ground-based datasets (Global Snow Monitoring for Climate Research-Version 3 (GlobSnow-v3) and European Space Agency Snow Climate Change Initiative-Version 2 (SnowCCI-v2)). The overestimation occurs in every year from 1982 to 2014 (Supplementary Fig. 1). This snow water resources paradox is manifested as an overestimation of SWE by the CMIP6 models across 61% of the NH land surface (Fig. 1c, blue regions) despite substantial underestimation of freezing day frequency.

A recent study found that the positive bias in SWE is related to a positive bias in precipitation during the accumulation season, while the effect of temperature is minimal, especially in the coldest regions[5]. Given the overestimation of precipitation and the underestimation of freezing day frequency, we hypothesize that the abnormally high SWE in CMIP6 models (Fig. 1c) might be due to an incorrect representation of snowfall (intensity and frequency). Using the Global Precipitation Climatology Centre (GPCC) daily precipitation data, we estimate the intensities and frequencies of light (1–10 kg m^{-2} d^{-1}), moderate (10–30 kg m^{-2} d^{-1}) and heavy (≥30 kg m^{-2} d^{-1}; Methods) snowfall for the period 1982–2014. We find that the CMIP6 models overestimate the total snowfall amount by 1,530 Gt. Although the simulated moderate and heavy snowfall amounts are close to those observed, the simulated light snowfall amount (5,859 ± 1,050 Gt) is overestimated by 28.3% or 1,293 Gt, relative to the GPCC estimate (4,566 ± 185 Gt; Fig. 1a; $P < 0.05$). Using other daily precipitation datasets from the Climate Prediction Center (CPC) and the Multi-Source Weighted-Ensemble Precipitation (MSWEP) to estimate light snowfall, we again show that the CMIP6 models overestimate the light snowfall amount (Supplementary Text 1 and Supplementary Fig. 2). A quantitative analysis of the mechanisms further indicates that total snowfall is the primary contributor to NH mean SWE biases, accounting for 91.5% of the total bias. Among the components of total snowfall, light snowfall contributes the most to SWE biases at 69.5 ± 9.8%, followed by moderate snowfall (11.1 ± 6.9%) and heavy snowfall (10.9 ± 3.1%). The remaining SWE bias primarily stems from snowmelt water (8.5%). We therefore conclude that the overestimation of light snowfall is the dominant factor underlying the snow water resources paradox. The monthly scale analysis (Supplementary Text 2 and Supplementary Figs. 3–5) and the analysis of the Land Surface, Snow and Soil Moisture Model Intercomparison Project (LS3MIP) CMIP6 offline experiment (Supplementary Text 3 and Supplementary Figs. 6–9) both support the dominant role of the light snowfall bias in contributing to the positive SWE bias, while snow melting physics also plays a critical role, particularly during the snow ablation period. While land–atmosphere coupling is not a primary factor contributing to the NH mean SWE bias, its impact can be significant in specific regions.

This conclusion regarding the dominant role of light snowfall bias in contributing to the positive SWE bias is further supported by the highly consistent geographical distributions of the overestimated SWE (Fig. 1c), light snowfall amount (Fig. 1d) and light snowfall frequency (Fig. 1e). Further analysis indicates that snowfall intensity (mean snowfall per snow day) is virtually identical in CMIP6 models and observations (2.98 ± 0.04 mm d^{-1} versus 3.00 ± 0.24 mm d^{-1}, respectively), but that the CMIP6 models significantly overestimate light snowfall frequency (31.0 ± 4.4 days per year), a bias of +27.0% or 6.6 days per year compared with observed values (24.4 ± 0.8 days per year, $P < 0.05$). This substantial bias in light snowfall frequency causes about 67.9% of the NH mean SWE bias, and far exceeds that of snowfall intensity (1.6%). Our regional analysis further supports this finding (Supplementary Text 4). However, it also highlights the critical roles of snowmelt processes, heavy snowfall and snowfall intensity in certain areas (Supplementary Fig. 10).

In contrast, in some regions, particularly in central eastern Siberia, SWE has increased even with rising temperatures due to the atmospheric dynamic-induced moisture convergence. Therefore, in these areas specifically, the occurrence of a positive bias in SWE in the ESMs is reasonable and not necessarily a paradox. On the other hand, some recent studies have raised concerns that very high resolution regional models may be too cold in high surface elevation regions to produce sufficient SWE[38–40], leading to a negative SWE bias that contrasts with the positive bias in CMIP6 models. The negative SWE bias in regional models probably arises from the underestimation of precipitation (including snowfall)[38], whereas the positive SWE bias in CMIP6 models is mainly attributed to an overestimation of light snowfall. Both cases emphasize the critical role of precipitation in SWE simulations.

Future freezing day frequency and SWE

Projections of freezing day frequency (Supplementary Fig. 11a,b) and SWE (Supplementary Fig. 11c,d) during the extended NH cold season both exhibit large differences across the CMIP6 models in the mid- (2041–2060) and long term (2081–2100). For example, the models

https://doi.org/10.1038/s41558-025-02308-y

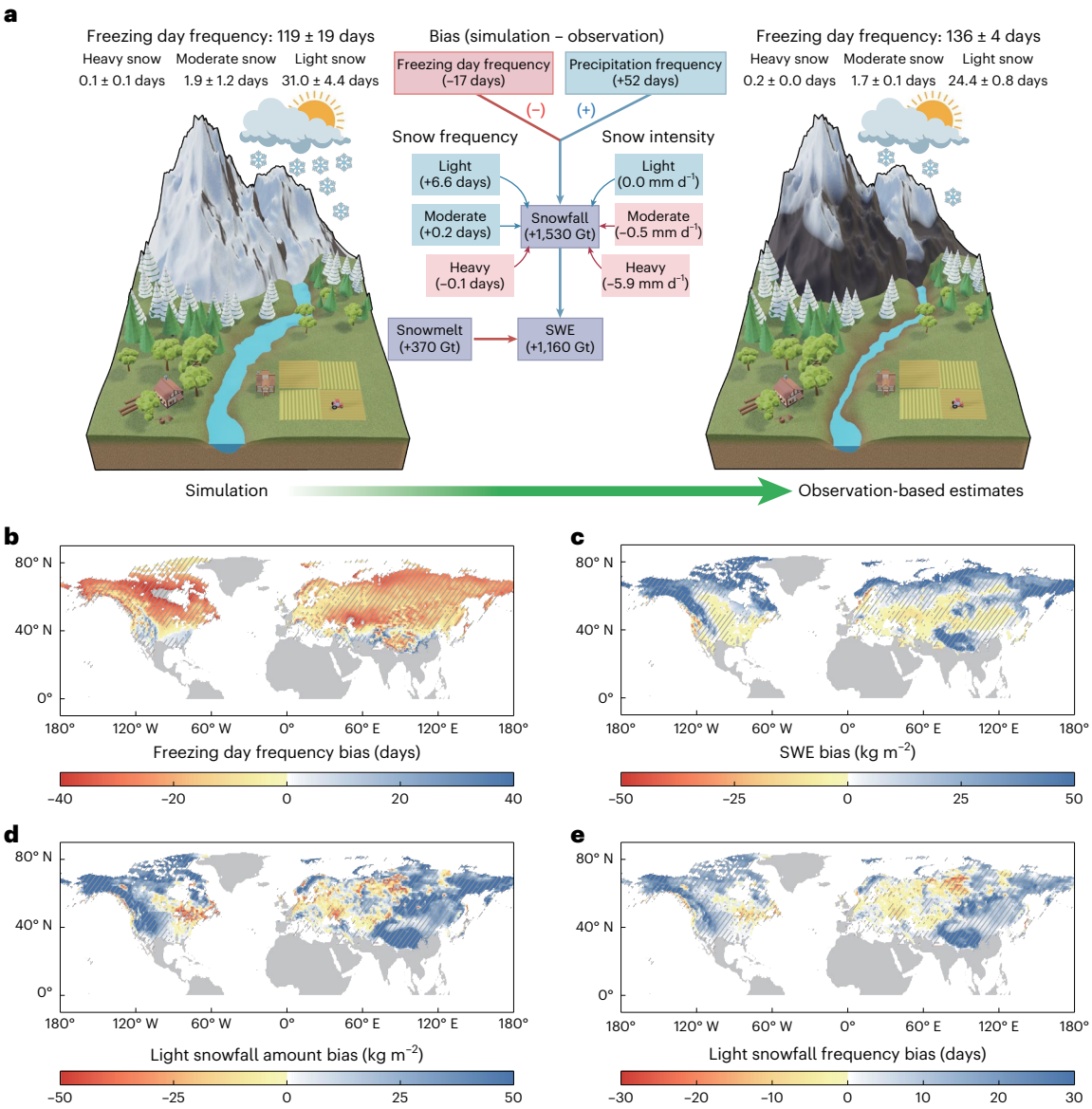

Fig. 1 | Characteristics and mechanisms of the snow water resources paradox in the extended NH cold season for the period 1982–2014. Regions without seasonal snow cover are excluded (grey areas). **a**, Relationships among temperature, snowfall, SWE and snowmelt water based on observation-based datasets and CMIP6 simulations. The snowfall frequency represents the multi-year average occurrence of light (1–10 kg m^{-2} d^{-1}), moderate (10–30 kg m^{-2} d^{-1}) and heavy (≥30 kg m^{-2} d^{-1}) snowfall. Blue arrows indicate that a variable (for example, overestimated snowfall) can increase the amount of the next variable (for example, overestimated SWE); red arrows indicate a decreasing effect. Snow sublimation is excluded due to its minimal impact on snow water resources compared with snowfall and snowmelt. **b**–**e**, Biases (CMIP6 minus observation-based estimates) in the multi-year average freezing day frequency (**b**), SWE (**c**), light snow amount (**d**) and light snowfall frequency (1–10 kg m^{-2} d^{-1}; **e**). Blue regions indicate overestimation by the ESMs, while red regions show underestimation. Regions with oblique lines demonstrate statistically significant differences between CMIP6 models and observation-based estimates ($P < 0.05$) as determined by a two-sided t-test. Maps in **b**–**e** generated using MATLAB R2022b.

project multi-year average mid-term future freezing day frequency and future SWE of 43.5–132.8 days (minimum–maximum) and 1,458–6,379 Gt respectively under SSP245. Using the emergent constraints, we obtain constrained estimates of future freezing day frequency and SWE with reduced uncertainty.

We first examine the emergent relationships between historical and future freezing day frequency across the CMIP6 models at each grid cell under four emission scenarios, and similarly consider such relationships for SWE. We find that the relationships for freezing day frequency (Fig. 2a and Supplementary Fig. 12) and SWE (Fig. 2b and Supplementary Fig. 13) are both statistically significant across more than nine-tenths of the NH ($P < 0.05$). This provides a basis for producing observationally constrained projections of future freezing day frequency and SWE conditions across much of the NH. The remaining regions, which either have insignificant relationships ($P > 0.05$; Fig. 2a,b) or snow-free conditions throughout the year, are excluded from the following analysis. This approach (focusing on the projection of a variable onto itself)[24] has also been used to constrain projections of future CO_2 concentrations[41] and the ratio of transpiration to evapotranspiration[42].

These relationships allow us to use observation-based estimates to constrain future freezing day frequency and SWE (Methods). We estimated the observed freezing day frequency from the Berkeley Earth temperature product that incorporates more temperature observations (over 40,000 records) than other available products[37]. Other data products provide highly consistent results (Supplementary Fig. 14).

https://doi.org/10.1038/s41558-025-02308-y

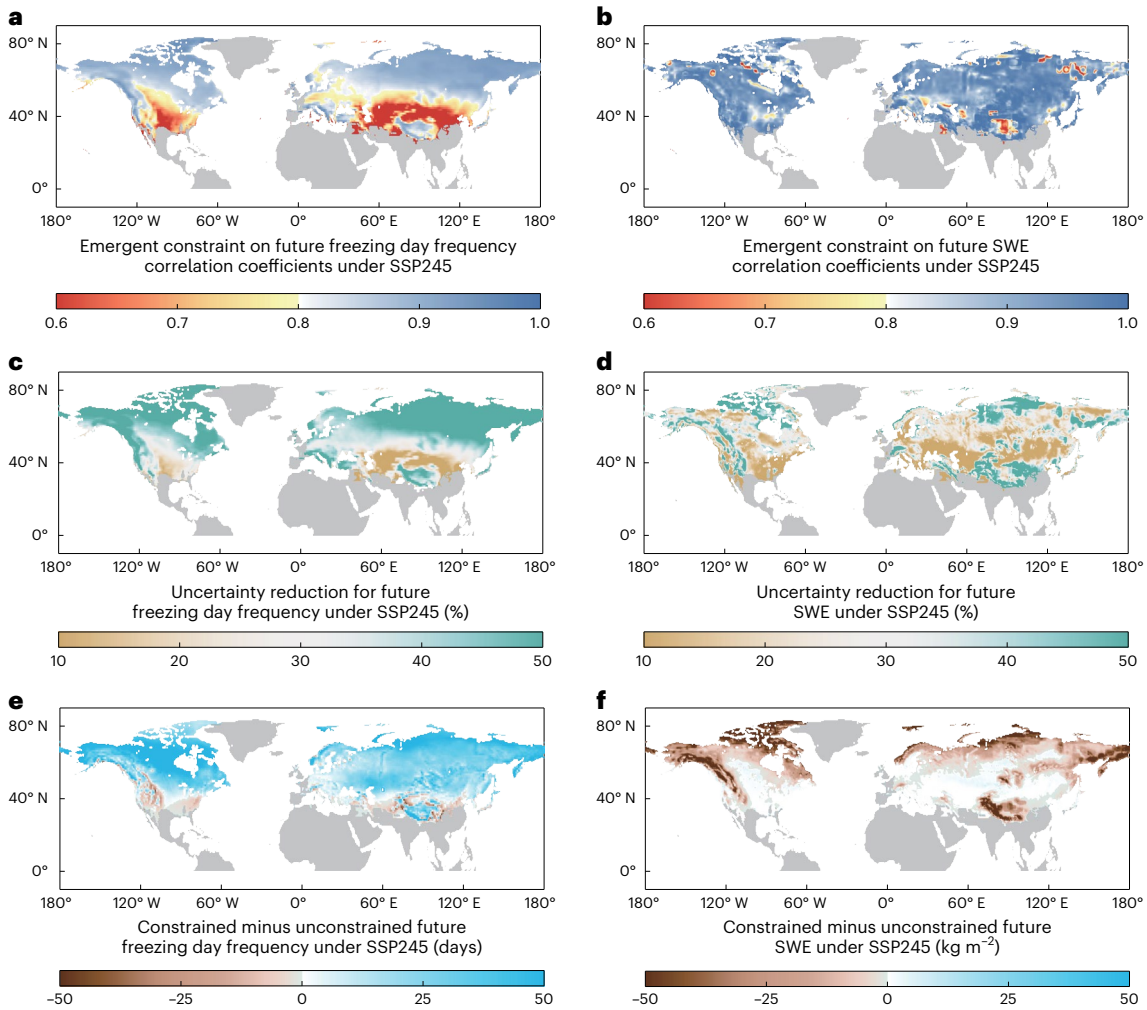

Fig. 2 | Observationally constrained projections of mean freezing day frequency and mean SWE in the extended NH cold season for the period 2041–2060 under SSP245 at the grid level. Regions without seasonal snow cover are excluded (grey areas). **a**, Pearson's correlation coefficients of emergent relationships between historical (1982–2014) and future (mid-term future period 2041–2060) simulations of mean freezing day frequency across the CMIP6 models. **b**, Correlation coefficients of emergent relationships between historical and mid-term future SWE simulations across the CMIP6 models. **c**, Percentage of uncertainty reduction for future mean freezing day frequency, relative to the original CMIP6 projections. **d**, Percentage of uncertainty reduction for future mean SWE. **e**, Constrained future mean freezing day frequency minus unconstrained future mean freezing day frequency. Brown regions indicate an overestimation of future mean freezing day frequency by ESMs, while blue regions show an underestimation. **f**, Constrained future mean SWE minus unconstrained future mean SWE. Emergent constraints on future freezing day frequency use the Berkeley Earth temperature product. Emergent constraints on future SWE use the nine SWE datasets (derived from GlobSnow-v3, SnowCCI-v2, MERRA-2, ERA5-Land, GLDAS-v2, NCEP2, FLDAS, CFSR and ERA5) and account for observational uncertainty by using the spread across observation-based products. Maps generated using MATLAB R2022b.

Applying the constraints substantially narrows the spread of freezing day frequency projections from the CMIP6 models over 90% of the NH's land surface under SSP245 for the mid-term projections (Fig. 2c), with the projected ranges significantly reducing from 64–138 days (mean ± 1 s.d.) to 99–141 days ($P < 0.01$). Application of the constraint at each grid cell, therefore, decreases projection uncertainty by 41%. Similar uncertainty reductions of 42–62% are obtained under the four emission scenarios in both the mid- and long-term future projections (Supplementary Fig. 15). Figure 2e suggests that the CMIP6 models underestimate the mid-term NH freezing day frequency by 16% under SSP245, with best estimates increasing from the original projections of 101 ± 37 days to the constrained results of 120 ± 21 days. This apparent underestimation occurs across more than nine-tenths of the NH's land surface. The underestimation of future freezing day frequency is consistently seen across the four SSPs in the mid-term projections (by 16–19%, depending on SSP) and in the long-term projections (12–13%; Supplementary Fig. 16).

In contrast with freezing day frequency, there is greater uncertainty amongst the long-term observation-based SWE datasets (Supplementary Fig. 11) due to the sparsity of in situ observations, simplified descriptions of physical snow processes, different retrieval algorithms, satellite data uncertainties and land surface model forcing uncertainty[6,43–45]. We therefore apply a hierarchical emergent constraint framework[46] (Methods) to account for the observational uncertainty in SWE across nine observation-based datasets and to constrain future SWE projections. The resulting constraint reduces the uncertainty of future mid-term NH mean SWE by 39% under SSP245, with the projected ranges reducing from 965–4,587 Gt to 967–3,177 Gt ($P < 0.01$). Similar uncertainty reductions of 36–39% (depending on the SSP) are obtained at mid-term under the other SSPs (Supplementary Fig. 17). The constraints provide uncertainty reductions of 25–34% in the long-term projections under the four SSPs (Supplementary Fig. 17). The largest uncertainty reductions are obtained in the snow-abundant regions of the Tibetan Plateau and the northern high latitudes (>50° N;

https://doi.org/10.1038/s41558-025-02308-y

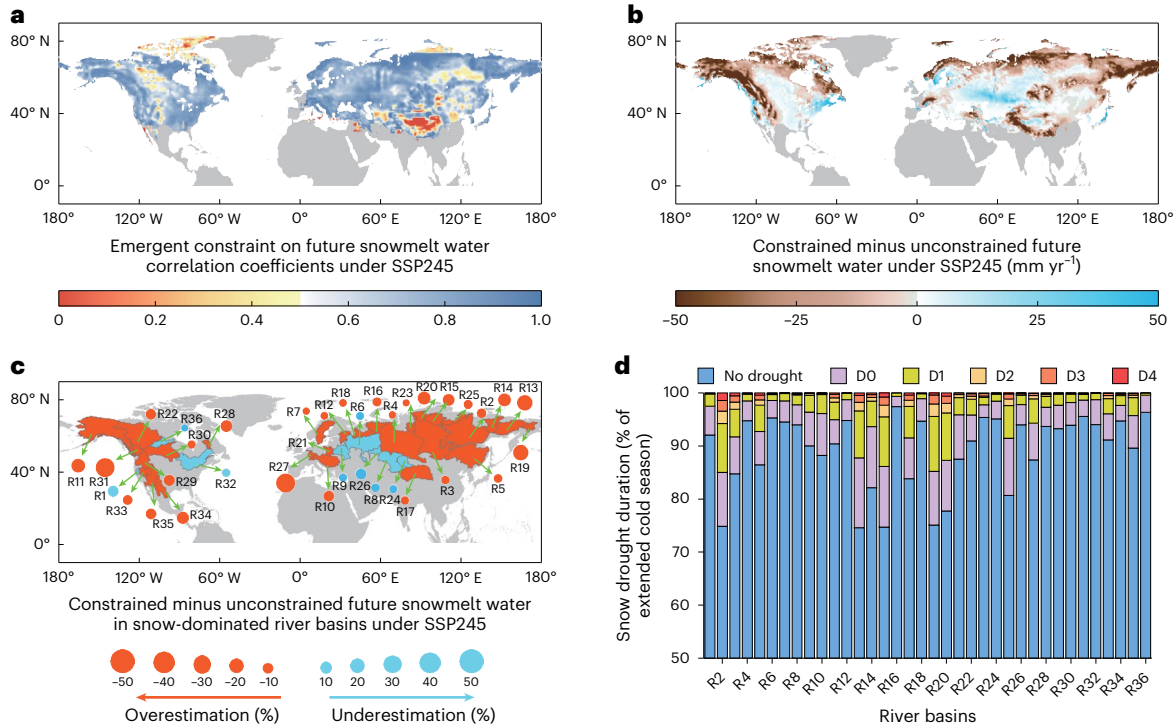

Fig. 3 | Implications for future annual mean snowmelt water in the NH under SSP245 for the period 2041–2060 at the grid level. a, Correlation coefficients for the emergent relationship between future SWE and future snowmelt water in each grid cell. **b**, Constrained future snowmelt water minus unconstrained future snowmelt water. **c**, Constrained future snowmelt water minus unconstrained results in the 36 snow-dominated regions. Orange circles represent overestimation of future snowmelt water by the CMIP6 models, and blue circles represent underestimation of future snowmelt water. For names of river basins, see Supplementary Tables 5 and 6. The regions with insignificant emergent relationships ($P > 0.05$) and with snow-free conditions throughout the year are excluded. **d**, Snow drought durations as a proportion of the extended cold season under SSP245 for mid-term future projections. D0, D1, D2, D3 and D4 correspond to abnormally dry, moderate drought, severe drought, extreme drought and exceptional drought, respectively (refer to the definitions in Supplementary Table 7). Maps in **a**–**c** generated using MATLAB R2022b.

Fig. 2c, d). In contrast with freezing day frequency, the application of our emergent constraint to SWE significantly decreases raw model projections of mid-term SWE under SSP245 from 2,776 ± 1,811 Gt to 2,072 ± 1,105 Gt ($P < 0.01$), indicating that models probably overestimate future SWE by 34% (Fig. 2f). Consistent results are obtained for the mid-term period and for the long-term period under the four SSPs, with SWE overestimated by 28–34% (Supplementary Fig. 18). The localized results show that the unconstrained ensemble overestimates SWE across more than half of the NH's land surface (Fig. 2f and Supplementary Fig. 18). The fact that the constraints increase the raw freezing day projections and decrease the raw SWE projections suggests that the snow water resources paradox persists in the future projections. Further investigation using a variety of approaches, including multi-scale consistency, out-of-sample testing in CMIP5 and model-based cross-validation[47,48] (Supplementary Text 5), confirms the robustness of these constrained projections.

Mechanisms of the snow water resources paradox in the future

To investigate the mechanisms underpinning the paradox in the projections, we examined the emergent relationships between historical and future simulations of light snow frequency and found that the relationships were significant over approximately nine-tenths of the NH's land surface ($P < 0.05$; Supplementary Fig. 23). Combining the observed estimates of light snow frequency from the GPCC product, we found that the CMIP6 models overestimate the mid-term future light snow frequency by 26–28% (Supplementary Fig. 24), with the original projections of 24.3 ± 10.6 days (SSP126), 24.5 ± 10.5 days (SSP245), 23.9 ± 10.5 days (SSP370) and 23.2 ± 10.5 days (SSP585) decreasing to the constrained values of 19.3 ± 7.6 days, 19.1 ± 7.8 days, 18.8 ± 7.8 days and 18.2 ± 7.6 days, respectively. In the long-term future projections, we again found an overestimation of 24–28%. Importantly, the overestimation (Supplementary Fig. 24) is mainly located in the regions where the future snow water resources paradox exists (Fig. 2f). This implies that the overestimation of future light snow frequency is the principal reason for the future snow water resources paradox. A fundamental mechanism may be related to the climate model bias towards the frequency of light precipitation (that is, the 'drizzle problem'; Supplementary Text 6)[49–56].

A greater potential threat to water resources

The snow water resources paradox affects snowmelt water, as reflected by the significant relationships between hemispheric average future SWE and snowmelt water across the CMIP6 models ($0.88 \le R \le 0.93$; Supplementary Fig. 25 and Supplementary Table 4). Thus, by diagnosing and applying the relationship between future projections of SWE and future snowmelt water, it may be possible to use the constrained future SWE to provide a meaningful constraint on future snowmelt water based on the traditional emergent constraint method. Previous studies have also applied this method of using constrained estimates to refine the other projected climate variables[4,28,31,42].

We examined the relationship between future SWE and snowmelt water in each grid cell and found that they remain statistically significant over nine-tenths of the NH's land surface ($P < 0.05$; Fig. 3a and Supplementary Fig. 26). Combining these relationships with the gridded constrained results of future SWE shows that the constrained estimate of future NH snowmelt water shifts from the raw CMIP6 projections of 150 ± 33 mm yr^{-1} (under SSP245) to 132 ± 20 mm yr^{-1} during the mid-term

future period. This indicates that the CMIP6 models probably overestimate NH snowmelt water by 12–16% under the four SSPs in both mid- and long-term future projections. The overestimation affects over half of the total NH area (Fig. 3b and Supplementary Fig. 27), especially in the snow-abundant regions of northern North America (overestimated by 22–29%), eastern Asia (20–27%) and the Tibetan Plateau (9–14%). Applying this two-stage constraint also lowers the uncertainty of future snowmelt water projections, with the uncertainty reduced by 33–37%. This indicates that the future snowmelt water supply risk is likely to be underestimated if the persistence of the snow water resources paradox is ignored and unadjusted ESM projections are employed.

To provide more meaningful information for water resources management at the basin scale, we applied the emergent relationships between future SWE and snowmelt water in 36 large snow-dominated river basins (≥70,000 km^2 based on the HydroBASINS dataset[57]; Supplementary Tables 5 and 6)[12]. The constrained results show that CMIP6 models are likely to statistically overestimate future snowmelt water in 25–28 of these basins (Fig. 3c, and Supplementary Tables 5 and 6; $P < 0.01$). To enhance the evaluation of potential snow water resource shortages in these river basins, we employed the standardized snow water equivalent index (Supplementary Text 7) to assess future risks of snow water resource deficits based on the constrained future SWE. Our findings indicate that snow water shortages are likely to become more severe in the future, with more regions facing the risk of extreme drought (Supplementary Text 8). In the Arctic region, including the Kolyma, Pyasina and Mackenzie river basins, varying degrees of snow drought (Fig. 3d and Supplementary Fig. 29) could impact dissolved organic carbon and nutrient transport, threatening the sustainability of Arctic ecosystems and altering carbon cycle dynamics in the Arctic shelf and ocean. For river basins like the Caniapiscau and Colorado, where economic development relies heavily on hydropower[11], our constrained projections suggest prolonged snow drought (Fig. 3d and Supplementary Fig. 29). The Fraser River, crucial for Pacific Ocean salmon populations, also faces high snow drought risks, potentially affecting salmon migrations. The Rhine River basin, heavily influenced by meltwater, faces remarkable snow drought risk, with severe drought (D2) and worse (extreme (D3) and exceptional (D4) drought) lasting for up to 25.4% of the extended cold season under SSP585. Conversely, river basins in northeastern Asia, such as the Lena (18.5–51.1% of the cold season), Amur (8.3–55.3%) and Kolyma (18.9–34.4%), show shorter durations of snow drought with a relatively stable standardized snow water equivalent index, indicating lesser impacts compared with other regions. This is attributed to the increased atmospheric moisture holding capacity and moisture convergence induced by atmospheric dynamics[15].

Online content

Any methods, additional references, Nature Portfolio reporting summaries, source data, extended data, supplementary information, acknowledgements, peer review information; details of author contributions and competing interests; and statements of data and code availability are available at https://doi.org/10.1038/s41558-025-02308-y.

References

1. Tokarska, K. B. et al. Past warming trend constrains future warming in CMIP6 models. *Sci. Adv.* **6**, eaaz9549 (2020).
2. McBride, L. A. et al. Comparison of CMIP6 historical climate simulations and future projected warming to an empirical model of global climate. *Earth Syst. Dyn.* **12**, 545–579 (2021).
3. Papalexiou, S. M. et al. Robustness of CMIP6 historical global mean temperature simulations: trends, long-term persistence, autocorrelation, and distributional shape. *Earths Future* **8**, e2020EF001667 (2020).
4. Chai, Y. et al. Constrained CMIP6 projections indicate less warming and a slower increase in water availability across Asia. *Nat. Commun.* **13**, 4124 (2022).
5. Kouki, K. et al. Evaluation of Northern Hemisphere snow water equivalent in CMIP6 models during 1982–2014. *Cryosphere* **16**, 1007–1030 (2022).
6. Mudryk, L. et al. Historical Northern Hemisphere snow cover trends and projected changes in the CMIP6 multi-model ensemble. *Cryosphere* **14**, 2495–2514 (2020).
7. Zhu, X. et al. Historical evolution and future trend of Northern Hemisphere snow cover in CMIP5 and CMIP6 models. *Environ. Res. Lett.* **16**, 065013 (2021).
8. Santolaria-Otín, M. & Zolina, O. Evaluation of snow cover and snow water equivalent in the continental Arctic in CMIP5 models. *Clim. Dyn.* **55**, 2993–3016 (2020).
9. Connolly, R. et al. Northern Hemisphere snow-cover trends (1967–2018): a comparison between climate models and observations. *Geosciences* **9**, 135 (2019).
10. Arheimer, B., Donnelly, C. & Lindström, G. Regulation of snow-fed rivers affects flow regimes more than climate change. *Nat. Commun.* **8**, 62 (2017).
11. Musselman, K. N. et al. Winter melt trends portend widespread declines in snow water resources. *Nat. Clim. Change* **11**, 418–424 (2021).
12. Barnett, T. P., Adam, J. C. & Lettenmaier, D. P. Potential impacts of a warming climate on water availability in snow-dominated regions. *Nature* **438**, 303–309 (2005).
13. Steppuhn, H. in *Handbook of Snow: Principles, Processes, Management and Use* (eds Gray, D. M. & Male, D. H.) 60–126 (Pergamon, 1981).
14. Thackeray, C. W. et al. Quantifying the uncertainty in historical and future simulations of Northern Hemisphere spring snow cover. *J. Clim.* **29**, 8647–8663 (2016).
15. Wang, Z. et al. Reasons for east Siberia winter snow water equivalent increase in the recent decades. *Remote Sens.* **15**, 134 (2022).
16. Berghuijs, W. R., Woods, R. A. & Hrachowitz, M. A precipitation shift from snow towards rain leads to a decrease in streamflow. *Nat. Clim. Change* **4**, 583–586 (2014).
17. Qin, Y. et al. Agricultural risks from changing snowmelt. *Nat. Clim. Change* **10**, 459–465 (2020).
18. Armstrong, R. L. & Brodzik, M. J. Recent Northern Hemisphere snow extent: a comparison of data derived from visible and microwave satellite sensors. *Geophys. Res. Lett.* **28**, 3673–3676 (2001).
19. Ren, Y. & Liu, S. Different influences of temperature on snow cover and sea ice area in the Northern Hemisphere. *Geogr. Res.* **37**, 870–882 (2018).
20. Nitta, T. et al. Representing variability in subgrid snow cover and snow depth in a global land model: offline validation. *J. Clim.* **27**, 3318–3330 (2014).
21. Shi, H. X. & Wang, C. H. Projected 21st century changes in snow water equivalent over Northern Hemisphere landmasses from the CMIP5 model ensemble. *Cryosphere* **9**, 1943–1953 (2015).
22. Hawkins, E. & Sutton, R. The potential to narrow uncertainty in projections of regional precipitation change. *Clim. Dyn.* **37**, 407–418 (2011).
23. Menard, C. B. et al. Scientific and human errors in a snow model intercomparison. *Bull. Am. Meteorol. Soc.* **102**, E61–E79 (2021).
24. Hall, A. et al. Progressing emergent constraints on future climate change. *Nat. Clim. Change* **9**, 269–278 (2019).
25. Klein, S. A. & Hall, A. Emergent constraints for cloud feedbacks. *Curr. Clim. Change Rep.* **1**, 276–287 (2015).
26. Brient, F. Reducing uncertainties in climate projections with emergent constraints: concepts, examples and prospects. *Adv. Atmos. Sci.* **37**, 1–15 (2020).
27. Williamson, M. S. et al. Emergent constraints on climate sensitivities. *Rev. Mod. Phys.* **93**, 025004 (2021).

28. Chai, Y. et al. Using precipitation sensitivity to temperature to adjust projected global runoff. *Environ. Res. Lett.* **16**, 124032 (2021).
29. Cox, P. M., Huntingford, C. & Williamson, M. S. Emergent constraint on equilibrium climate sensitivity from global temperature variability. *Nature* **553**, 319–322 (2018).
30. Cox, P. et al. Sensitivity of tropical carbon to climate change constrained by carbon dioxide variability. *Nature* **494**, 341–344 (2013).
31. Chai, Y. et al. Constraining Amazonian land surface temperature sensitivity to precipitation and the probability of forest dieback. *npj Clim. Atmos. Sci.* **4**, 6 (2021).
32. Hall, A. & Qu, X. Using the current seasonal cycle to constrain snow albedo feedback in future climate change. *Geophys. Res. Lett.* **33**, L03502 (2006).
33. Thackeray, C. W. & Hall, A. An emergent constraint on future Arctic sea-ice albedo feedback. *Nat. Clim. Change* **9**, 972–978 (2019).
34. Terhaar, J., Kwiatkowski, L. & Bopp, L. Emergent constraint on Arctic Ocean acidification in the twenty-first century. *Nature* **582**, 379–383 (2020).
35. Sherwood, S. C., Bony, S. & Dufresne, J. L. Spread in model climate sensitivity traced to atmospheric convective mixing. *Nature* **505**, 37–42 (2014).
36. DeAngelis, A. M. et al. An observational radiative constraint on hydrologic cycle intensification. *Nature* **528**, 249–253 (2015).
37. Rohde, R. A. & Hausfather, Z. The Berkeley Earth land/ocean temperature record. *Earth Syst. Sci. Data* **12**, 3469–3479 (2020).
38. He, C. et al. Can convection-permitting modeling provide decent precipitation for offline high-resolution snowpack simulations over mountains? *J. Geophys. Res. Atmos.* **124**, 12631–12654 (2019).
39. Rasmussen, R. M. et al. CONUS404: the NCAR–USGS 4-km long-term regional hydroclimate reanalysis over the CONUS. *Bull. Am. Meteorol. Soc.* **104**, E1382–E1408 (2023).
40. Rudisill, W., Rhoades, A., Xu, Z. & Feldman, D. R. Are atmospheric models too cold in the mountains? The state of science and insights from the SAIL field campaign. *Bull. Am. Meteorol. Soc.* **105**, E1237–E1264 (2024).
41. Hoffman, F. M. et al. Causes and implications of persistent atmospheric carbon dioxide biases in Earth system models. *J. Geophys. Res. Biogeosci.* **119**, 141–162 (2014).
42. Lian, X. et al. Partitioning global land evapotranspiration using CMIP5 models constrained by observations. *Nat. Clim. Change* **8**, 640–646 (2018).
43. Mortimer, C. et al. Evaluation of long-term Northern Hemisphere snow water equivalent products. *Cryosphere* **14**, 1579–1594 (2020).
44. Mudryk, L. R. et al. Characterization of Northern Hemisphere snow water equivalent datasets, 1981–2010. *J. Clim.* **28**, 8037–8051 (2015).
45. Pulliainen, J. et al. Patterns and trends of Northern Hemisphere snow mass from 1980 to 2018. *Nature* **581**, 294–298 (2020).
46. Bowman, K. W. et al. A hierarchical statistical framework for emergent constraints: application to snow-albedo feedback. *Geophys. Res. Lett.* **45**, 13050–13059 (2018).
47. Annan, J. D. & Hargreaves, J. C. Reliability of the CMIP3 ensemble. *Geophys. Res. Lett.* **37**, L02803 (2010).
48. Schurer, A. et al. Estimating the transient climate response from observed warming. *J. Clim.* **31**, 8645–8663 (2018).
49. Shamekh, S. et al. Implicit learning of convective organization explains precipitation stochasticity. *Proc. Natl Acad. Sci. USA* **120**, e2216158120 (2023).
50. Chen, D. & Dai, A. Precipitation characteristics in the Community Atmosphere Model and their dependence on model physics and resolution. *J. Adv. Model. Earth Syst.* **11**, 2352–2374 (2019).
51. Chen, D., Dai, A. & Hall, A. The convective-to-total precipitation ratio and the "drizzling" bias in climate models. *J. Geophys. Res. Atmos.* **126**, e2020JD034198 (2021).
52. Stephens, G. L. et al. Dreary state of precipitation in global models. *J. Geophys. Res. Atmos.* **115**, D24211 (2010).
53. Rosa, D. & Collins, W. D. A case study of subdaily simulated and observed continental convective precipitation: CMIP5 and multiscale global climate models comparison. *Geophys. Res. Lett.* **40**, 5999–6003 (2013).
54. Wilcox, E. M. & Donner, L. J. The frequency of extreme rain events in satellite rain-rate estimates and an atmospheric general circulation model. *J. Clim.* **20**, 53–69 (2007).
55. Kopparla, P. et al. Improved simulation of extreme precipitation in a high-resolution atmosphere model. *Geophys. Res. Lett.* **40**, 5803–5808 (2013).
56. Westra, S. et al. Future changes to the intensity and frequency of short-duration extreme rainfall. *Rev. Geophys.* **52**, 522–555 (2014).
57. Lehner, B. & Grill, G. Global river hydrography and network routing: baseline data and new approaches to study the world's large river systems. *Hydrol. Process.* **27**, 2171–2186 (2013).

Methods

ESM datasets

SWE, snowmelt water, temperature and precipitation during the historical (1982–2014) and future (2015–2100) periods were acquired from the CMIP6 models to derive the emergent relationships and to analyse the plausible mechanisms under the low- (SSP126), medium- (SSP245) and high-emission (SSP370 and SSP585) scenarios. Data for SWE were also acquired from the CMIP5 models under the Representative Concentration Pathway 45 and 85 emission scenarios to test the robustness of the emergent relationships. Here, we used one realization per model (that is, the first realization). We re-gridded all CMIP5 and CMIP6 outputs and observation-based datasets to a common 0.5° × 0.5° latitude–longitude spatial resolution. Effectively, glaciated grid cells occur in climate models when the annual accumulation of snowfall exceeds snowmelt and sublimation losses in high-elevation areas with low annual mean temperatures. While this tends to happen in reasonable locations where glaciers and ice sheets also exist in the real world (for example, along the coastal mountains of Alaska, at high-elevation regions of the Canadian Arctic, in High Mountain Asia, and over Greenland and Antarctica), the models do not explicitly distinguish between glaciers and seasonal snow. In some models, SWE can accumulate to large amounts over such grid cells (for example, greater than 500 kg m^{-2})[6]. Additionally, there is substantial inter-model variability in the maximum amount of snow each model accumulates. Therefore, neither the climatological mean SWE nor the trends accurately represent seasonal snow in the real world. To eliminate the effect of these 'glaciated' grid cells, we removed all SWE values greater than 500 kg m^{-2} in the CMIP6 models, following ref. 6.

Observation-based datasets

We used SWE data from nine datasets (GlobSnow-v3, SnowCCI-v2, MERRA-2, ERA5-Land, ERA5, CFSR, GLDAS-v2, FLDAS and NCEP2). The GlobSnow-v3 and SnowCCI-v2 datasets are satellite and ground-based datasets, while the remaining seven are reanalysis datasets. As mentioned earlier, for clarity, we refer to these two categories collectively as the observation-based estimates throughout the text. These datasets have been evaluated and extensively used for climatic and hydrological research and climate model evaluation[58–62]. The GlobSnow-v3 and SnowCCI-v2 datasets, which combine satellite-based passive microwave radiometer data with ground-based synoptic snow depth observations, provide SWE data[63,64]. The MERRA-2 dataset, which is a National Aeronautics and Space Administration atmospheric reanalysis dataset, has assimilated available in situ and satellite observations into a climate model since 1980, with a resolution of 0.625° × 0.5° (ref. 65). ERA5-Land[66] and ERA5[67] both use the Hydrology Tiled European Centre for Medium-Range Weather Forecasts Scheme for Surface Exchanges land surface model (HTESSEL) to provide reanalysed SWE datasets at resolutions of 0.75° × 0.75° and 0.25° × 0.25°, respectively. CFSR covers the period from 1979 to 2019, with 0.5° × 0.5° spatial resolution[8]. Proved to agree well with regional gauge-based observations[68–70], the CFSR dataset has been widely applied to estimate the observational characteristics of NH SWE, and it has also been used for calibration and validation of ESMs (for example, CMIP5 models)[71,72]. The GLDAS-v2 dataset uses advanced land surface modelling and data assimilation techniques to provide a temporally consistent series from 1948 to 2014, forced entirely with the Princeton meteorological forcing input data, with a resolution of 0.1° × 0.1° (ref. 73). FLDAS is simulated from the Noah 3.6.1 model in the Famine Early Warning Systems Network Land Data Assimilation System, with a resolution of 0.1° × 0.1° from January 1982 to the present[74]. The simulation uses MERRA-2 data and Climate Hazards Group InfraRed Precipitation with Station (CHIRPS) six-hourly rainfall data. The NCEP Reanalysis 2 project uses a frozen analysis/forecast system to perform data assimilation using past data from 1979 to the near-present with 2.5° × 2.5° spatial resolution[75]. Differences amongst these nine SWE datasets compared with 11,071 in situ SWE observation stations are discussed in Supplementary Text 9.

The Berkeley Earth land daily temperature record utilizes significantly more land station data (over 40,000 stations) compared with the other products[37], and is therefore used to estimate the observed freezing day frequency (that is, the number of days with temperature lower than 0 °C). The GPCC daily precipitation product is the most commonly used product that uses data acquired from more than 85,000 stations worldwide[76]. On days with freezing temperatures, observed light snowfall (1–10 kg m^{-2} d^{-1}), moderate snowfall (10–30 kg m^{-2} d^{-1}) and heavy snowfall (≥30 kg m^{-2} d^{-1}) are estimated based on the GPCC data. The choice of temperature threshold for determining freezing days is critical, particularly in conditions near freezing, and this is especially important for estimating light snowfall. We conducted an uncertainty analysis on the impact of temperature thresholds on light snowfall estimates and found that the selection of different thresholds did not affect our conclusions (Supplementary Text 10).

Hierarchical emergent constraint framework

The hierarchical emergent constraint framework applied here explicitly relates future climate, current climate and observations through conditional probability distributions[46]. This method allows us to fully consider the observational uncertainty across the nine SWE datasets. The core of the emergent constraint method is to identify a strong statistical relationship between an element x of the observable climate and an important variable y describing the future simulated state (equation (1)), across an ESM ensemble[46]. Once diagnosed from an ensemble of models, this emergent relationship can be applied to the observed value of x to produce a more reliable and accurate future climate projection for y (equations (3) and (4))[77]. When certain models estimate particularly anomalous SWE, these anomalous values can impact the effectiveness of the emergent constraint, requiring their removal. We used the Z-score method to identify outlier models: if the estimated value from a given model simulation exceeds three times the standard deviation from the mean, it is classified as an outlier. The details of the method are described in ref. 46.

$$y = a(x - \bar{x}) + \bar{y} \tag{1}$$

where a is obtained using equation (2), and $\bar{y}$ and $\bar{x}$ are the multi-model ensemble mean values of y and x, respectively. Here, ρ is the correlation coefficient between y and x; σ_y and σ_x are the standard deviations of y and x, respectively, across an ESM ensemble:

$$a = \rho \frac{\sigma_y}{\sigma_x} \tag{2}$$

The constrained future Earth system variable $\bar{y}_c$ and its variance can be estimated using equations (3) and (4), respectively:

$$\overline{y_c} = \bar{y} + \frac{a}{1 + \mathrm{SNR}^{-1}}(\overline{x_0} - \bar{x}) \tag{3}$$

$$\sigma^2_{y_c} = \left(1 - \frac{\rho^2}{1 + \mathrm{SNR}^{-1}}\right)\sigma^2_y \tag{4}$$

SNR, the signal-to-noise ratio, defines the relative strength of the signal variability to the noise variability[77], estimated by using equation (5), where σ^2_x and σ^2_o are the variances across the models and across the different observation-based datasets, respectively[77]:

$$\mathrm{SNR} = \frac{\sigma^2_x}{\sigma^2_o} \tag{5}$$

Model-based cross-validation

The question arises as to how we can determine whether the constrained projections are closer to the actual values compared with

their raw projections, given the absence of observational data for the future period. The model-based cross-validation method addresses this concern directly by selecting one of the CMIP6 models' projections of future SWE as a 'pseudo observation'[78]. The discrepancy in future SWE between the 'pseudo observation' and the multi-model mean estimate of the remaining CMIP6 models serves to estimate the raw bias in the CMIP6 projections. Subsequently, combining the 'pseudo observation' with the emergent relationship across the remaining CMIP6 models provides the constrained estimate of future SWE. The difference between the 'pseudo observation' and the constrained results represents the constrained bias after applying the emergent constraint. This process is repeated for each CMIP6 model at the grid-cell level, allowing us to compare the raw bias and the constrained bias in the SWE projections. There is confidence in the observationally constrained projection if the constrained pseudo-future projection has lower bias and uncertainty than the raw multi-model mean projection obtained from the ensemble of models that excludes the model that provided the pseudo observations of the past and future.

Data availability

The daily precipitation products from GPCC, CPC and MSWEP were derived from https://opendata.dwd.de/climate_environment/GPCC/full_data_daily_v2022/, https://psl.noaa.gov/data/gridded/data.cpc.globalprecip.html and https://www.gloh2o.org/mswep/, respectively. The daily temperature records from Berkeley Earth, ERA5-Land, MERRA-2 and the Japanese 55-year Reanalysis (JRA-55) were derived from https://berkeleyearth.org/data/, https://cds.climate.copernicus.eu/datasets/reanalysis-era5-land?tab=overview, https://gmao.gsfc.nasa.gov/reanalysis/MERRA-2/ and https://rda.ucar.edu/datasets/d628000/, respectively. The CMIP6 model simulations, including SWE, snowmelt water, precipitation and temperature, were acquired from https://esgf-node.llnl.gov/projects/cmip6/. The CMIP5 model simulations were acquired from https://esgf-node.llnl.gov/projects/cmip5/. The observation-based SWE datasets were acquired from GlobSnow-v3 (https://doi.org/10.1594/PANGAEA.911944)[79], SnowCCI-v2 (https://catalogue.ceda.ac.uk/uuid/93cf539bc3004cc8b98006e69078d86b/), MERRA-2 (https://gmao.gsfc.nasa.gov/reanalysis/MERRA-2/), ERA5-Land (https://cds.climate.copernicus.eu/cdsapp#!/dataset/reanalysis-era5-land-monthly-means?tab=overview), GLDAS-v2 (https://disc.gsfc.nasa.gov/datasets/GLDAS_CLSM10_M_2.0/summary?keywords=snow%20water%20equivalent), NCEP2 (https://psl.noaa.gov/data/gridded/data.ncep.reanalysis2.html), FLDAS (https://disc.gsfc.nasa.gov/datasets/FLDAS_NOAH01_C_GL_M_001/summary?keywords=snow%20water%20equivalent), CFSR (https://esgf-node.llnl.gov/search/create-ip/) and ERA5 (https://cds.climate.copernicus.eu/datasets/reanalysis-era5-single-levels-monthly-means?tab=overview). The Offline Land Model Experiment (LMIP) and the Prescribed Land Surface States (LFMIP) CMIP6 experiments, including SWE and snowmelt water, were derived from https://aims2.llnl.gov/search/cmip6/.

Code availability

Codes to reproduce the study are available via GitHub at https://github.com/alanchai/Overcoming-the-Northern-Hemisphere-snow-water-resources-paradox.git (ref. 80).

References

58. Reichle, R. H. et al. Assessment of MERRA-2 land surface hydrology estimates. *J. Clim.* **30**, 2937–2960 (2017).
59. Cortés, G., Girotto, M. & Margulis, S. Snow process estimation over the extratropical Andes using a data assimilation framework integrating MERRA data and Landsat imagery. *Water Resour. Res.* **52**, 2582–2600 (2016).
60. Lim, Y. K. et al. Atmospheric summer teleconnections and Greenland ice sheet surface mass variations: insights from MERRA-2. *Environ. Res. Lett.* **11**, 024002 (2016).
61. Saavedra, F. A. et al. Changes in Andes snow cover from MODIS data, 2000–2016. *Cryosphere* **12**, 1027–1046 (2018).
62. Huning, L. S. & AghaKouchak, A. Global snow drought hot spots and characteristics. *Proc. Natl Acad. Sci. USA* **117**, 19753–19759 (2020).
63. Luojus, K. et al. GlobSnow v3.0 Northern Hemisphere snow water equivalent dataset. *Sci. Data* **8**, 163 (2021).
64. Mortimer, C. et al. Benchmarking algorithm changes to the Snow CCI+ snow water equivalent product. *Remote Sens. Environ.* **274**, 112988 (2022).
65. Gelaro, R. et al. The Modern-Era Retrospective analysis for Research and Applications, version 2 (MERRA-2). *J. Clim.* **30**, 5419–5454 (2017).
66. Balsamo, G. et al. ERA-Interim/Land: a global land surface reanalysis data set. *Hydrol. Earth Syst. Sci.* **19**, 389–407 (2015).
67. Hoffmann, L. & Spang, R. An assessment of tropopause characteristics of the ERA5 and ERA-Interim meteorological reanalyses. *Atmos. Chem. Phys.* **22**, 4019–4046 (2022).
68. Sato, K. & Inoue, J. Comparison of Arctic sea ice thickness and snow depth estimates from CFSR with in situ observations. *Clim. Dyn.* **50**, 289–301 (2018).
69. Palerme, C. et al. Evaluation of Antarctic snowfall in global meteorological reanalyses. *Atmos. Res.* **190**, 104–112 (2017).
70. Brown, R., Tapsoba, D. & Derksen, C. Evaluation of snow water equivalent datasets over the Saint-Maurice River basin region of southern Québec. *Hydrol. Process.* **32**, 2748–2764 (2018).
71. Terzago, S. et al. Snowpack changes in the Hindu Kush–Karakoram–Himalaya from CMIP5 global climate models. *J. Hydrometeorol.* **15**, 2293–2313 (2014).
72. Iseri, Y. et al. Dynamical downscaling of global reanalysis data for high-resolution spatial modeling of snow accumulation/melting at the central/southern Sierra Nevada watersheds. *J. Hydrol.* **598**, 126445 (2021).
73. Rodell, M. et al. The global land data assimilation system. *Bull. Am. Meteorol. Soc.* **85**, 381–394 (2004).
74. McNally, A. *FLDAS Noah Land Surface Model L4 Global Monthly 0.1 × 0.1 degree (MERRA-2 and CHIRPS)* (Goddard Earth Sciences Data and Information Services Center, 2018); https://doi.org/10.5067/5NHC22T9375G
75. Kanamitsu, M. et al. NCEP–DOE AMIP-II Reanalysis (R-2). *Bull. Am. Meteorol. Soc.* **83**, 1631–1644 (2002).
76. Sun, Q. et al. A review of global precipitation data sets: data sources, estimation, and intercomparisons. *Rev. Geophys.* **56**, 79–107 (2018).
77. Chen, X. et al. Emergent constraints on future projections of the western North Pacific Subtropical High. *Nat. Commun.* **11**, 2802 (2020).
78. Li, C. et al. Constraining projected changes in rare intense precipitation events across global land regions. *Geophys. Res. Lett.* **51**, e2023GL105605 (2024).
79. Luojus, K. et al. GlobSnow v3.0 snow water equivalent (SWE) [dataset]. *PANGAEA* https://doi.org/10.1594/PANGAEA.911944 (2020).
80. Chai, Y. et al. Overcoming-the-Northern-Hemisphere-snow-water-resources-paradox. *GitHub* https://github.com/alanchai/Overcoming-the-Northern-Hemisphere-snow-water-resources-paradox.git (2024).

Acknowledgements

C.M. acknowledges support from the National Key Research and Development Program of China (2024YFF0809301) and the National Natural Science Foundation of China (U24A20572).

Y.C. acknowledges support from the National Natural Science Foundation of China (42301018). P.G. acknowledges National Science Foundation (NSF) LEAP Science and Technology Center award no. 2019625. L.S. acknowledges the UKRI FLF scheme (MR/V022008/1).

Author contributions

Y.C., C.M. and F.Z. led the writing, designed the research and performed the data analysis. P.G., L.M., C.W.T., W.R.B., Y.W., X.F., L.S. and Q.S. revised the paper and provided valuable comments.

Competing interests

The authors declare no competing interests.

Additional information

Supplementary information The online version contains supplementary material available at https://doi.org/10.1038/s41558-025-02308-y.

Correspondence and requests for materials should be addressed to Chiyuan Miao.

Peer review information *Nature Climate Change* thanks the anonymous reviewers for their contribution to the peer review of this work.